3D Printing of Multi-layer Magnetic Miniature Soft Robots with Programmable Magnetization

Zhaoxin Li, Yung Priscilla Lai, and Eric Diller*

Z. Li, Y.P. Lai and E. Diller
Department of Mechanical and Industrial Engineering, University of Toronto, 170 College St., Toronto, M5S 3E3, Canada
E-mail: lzx.lee@mail.utoronto.ca

Keywords: soft robots, magnetic actuation, digital light processing

Magnetically-driven miniature soft robots exhibit fast and dexterous responses to an applied external magnetic field. With remote manipulation, controlled navigation of robots can be realized within hard-to-access spaces for potential use in the human body. Existing magnetic miniature soft robots using digital light processing (DLP) are fabricated from planar sheets, and thus have limited shape transformations and locomotive behaviors. Here, we report a multi-layer three-dimensional (3D) printing method for patterning magnetic nanoparticles (MNPs) in ultraviolet (UV)-curable polymer matrix. Various multi-layer 3D structures within 10 millimeters in overall size are fabricated with controlled volumes at different parts, which outperform 2D folded shapes in terms of robustness and kinematic flexibility. By programming heterogeneous magnetization within discrete multi-layer robot segments, magnetic torque-induced shape changes including gripping, rolling, swimming and walking are induced by a global actuation field. Stacked design features with minimum dimension of 200 microns and encoded magnetization with resolution of 350 microns can be realized in the printing process. Meanwhile, enhanced deformation flexibility and formation of orientation-anchoring mechanisms are created by integrating multiple materials with distinct mechanical and magnetic properties, respectively, which enables the creation of versatile 3D multi-material actuators.

1. Introduction

Small-scale robots that can non-invasively access confined or hard-to-reach space have promising potential as non-invasive biomedical devices. To avoid a high level of complexity required to embed circuits and power sources on millimeter-to-micrometer scale robots, it is preferred to manufacture miniature robots that rely on stimuli-responsive materials which

induce robot deformations using changes in light, temperature, pH, pneumatic power, electric or magnetic field.[1] Among these, magnetically-driven soft robots exhibit faster response than devices made of shape memory polymers that are based on the light or thermal stimulus. Meanwhile, magnetic robots can be wirelessly controlled by the magnetic field, which outperform electric and pneumatic actuators in terms of untethered manipulation. Such fast, precise and dexterous response makes magnetic actuators promising miniaturized tools for biomedical use such as targeted drug delivery,[2-4] cell culture,[5,6] biofilm cleaning,[7] and minimally invasive intervention.[8-10]

Various types of 2D and 3D magnetic structures have been manufactured by two photon polymerization (TPP),[6,11-16] direct ink writing (DIW),[17-19] drop-on-demand 3D printing,[20] mold casting/jig-assisted printing,[5,11,12,21-23] continuous liquid interface production (CLIP),[24,25] fused deposition modeling (FDM)[26] and digital light processing (DLP).[27-31] However, additive manufacturing and programming of magnetization of magnetic materials on the micro scale remain challenging, especially for more sophisticated capabilities including multi-layer and multi-material fabrication.

Restrictions of using DLP involve the limitation on mass ratio of embedded magnetic nanoparticles (MNPs). The ratio of MNPs to bind polymer matrix needs to be low to maintain a high material transparency and crosslinked layer thickness. This low MNPs loading requirement will lead to a lower magnetic moment density of magnetoactive robot components compared with that using mold casting[21-23] or molding-integrated TPP.[11,12] The fabricated feature using TPP[6,11-16] can reach a scale of micrometer or nanometer, of which the resolution is higher than using DLP. However, other than coating MNPs on the polymeric skeleton[13,14] or preparing molds[11,12] using TPP, we can create magnetic structures more efficiently by directly patterning magnetic composite with MNPs loaded in the polymer matrix using DLP. Meanwhile, 3D structures can be produced at a higher throughput using DLP than mold casting[21-23] or jig-assisted printing.[5] For DIW, structural instability arises in filament stacking, so the rheological properties of the material should be tuned and supporting parts may need to be used as buttresses. Similarly, drop-on-demand 3D printing also requires tuning of the material's rheological properties. With DLP, no rheological modifications or external supports of materials are needed during layer stacking as it uses patterned light to cure layers of photoresponsive polymer. Therefore, multi-layer 3D magnetic structures on millimeter scale can be produced with high efficiency and reproducibility by directly patterning magnetic composite via the digitalized process of DLP, which provides a novel way of fabricating sophisticated multi-layer magnetic actuators, in the meantime, enabling the

production of versatile miniature structures that are based on photocurable stimuli-responsive materials.

The structural complexity of magnetic robots also gets enhanced in this work using the technique of DLP. Small-scale 3D structures that are manufactured using DLP in previous studies approximate each actuating part as a single magnetic point dipole, and use concentrated fields generated by an external permanent magnet to actuate the magnetoactive segment.[28,29] Such actuation schemes rely on the magnetic force generated by the permanent magnet in close proximity, where complex field changes such as oscillatory or periodic signals cannot be achieved, thus limiting the maneuverability for printed robots. Other than the magnetic force-induced deformation, shape morphing with higher complexity can be realized through magnetic torque-induced deformation. To achieve such sophistication, different techniques have been used for heterogeneous magnetization encoding or reprograming such as continuous magnetization,[22] local heating,[32,33] adhesive transfer printing,[34,35] switching field tailoring[36] or discrete magnetization patterning.[17-19,27]

With the techniques of fabrication and magnetization encoding discussed above, programmed shape transformation and controlled locomotion such as gripping,[27,28] crawling,[19,29,30,37] swimming,[2-4,7-9,13,14,22,38] metachronal waving[23,39] or multimodal behaviors[40] can be realized under magnetic actuation or manipulations combined with light,[2,41] thermal[18,42,43] or radio frequency (RF)[10] signals.

The complexity of structural design and magnetic polarity impacts the functionality of printed microrobots. With digital light processing (DLP), we have previously demonstrated the fabrication of 2D folded magnetic structures with programmed discrete magnetization,[27] and we also improved the design complexity by integrating multiple materials with different magnetic or mechanical properties.[44] However, single-layer robot shapes have limited performance in terms of structural flexibility and compliance compared with multi-layer 3D structures. For instance, volumes of joints and actuating parts of multi-layer structures can be adjusted by stacking features vertically during the printing process to get higher bending flexibility and greater actuating torques, respectively, which is unrealizable in single-layer fabrication. Building a volume through vertical stacking can also prevent the printed robot from capillary trapping which single-layer structures may suffer from during actuation. In addition, the structural and magnetic characteristics also depend on the types of materials the robot contains. The structural compliance and maneuverability can be enhanced by integrating rigid and flexible materials as well as incorporating magnetically soft and hard materials. Since the magnetic and mechanical characteristics are controlled by embedded MNPs and

polymer matrices, respectively, such properties can be engineered in parallel to enhance the functionalities for printed robots.

In this work, multi-layer magnetic shapes including stool-shaped, gripper-shaped, capsule-like, helical and walking robots were fabricated with encoded discretized magnetization patterns. Independent deformation of each actuating part and an overall complex shape changes were triggered by magnetic torque with a global actuating field generated by electromagnetic coils. Enhanced shape morphing and locomotion capabilities were observed by integrating materials with different magnetic and mechanical properties for the walking robot.

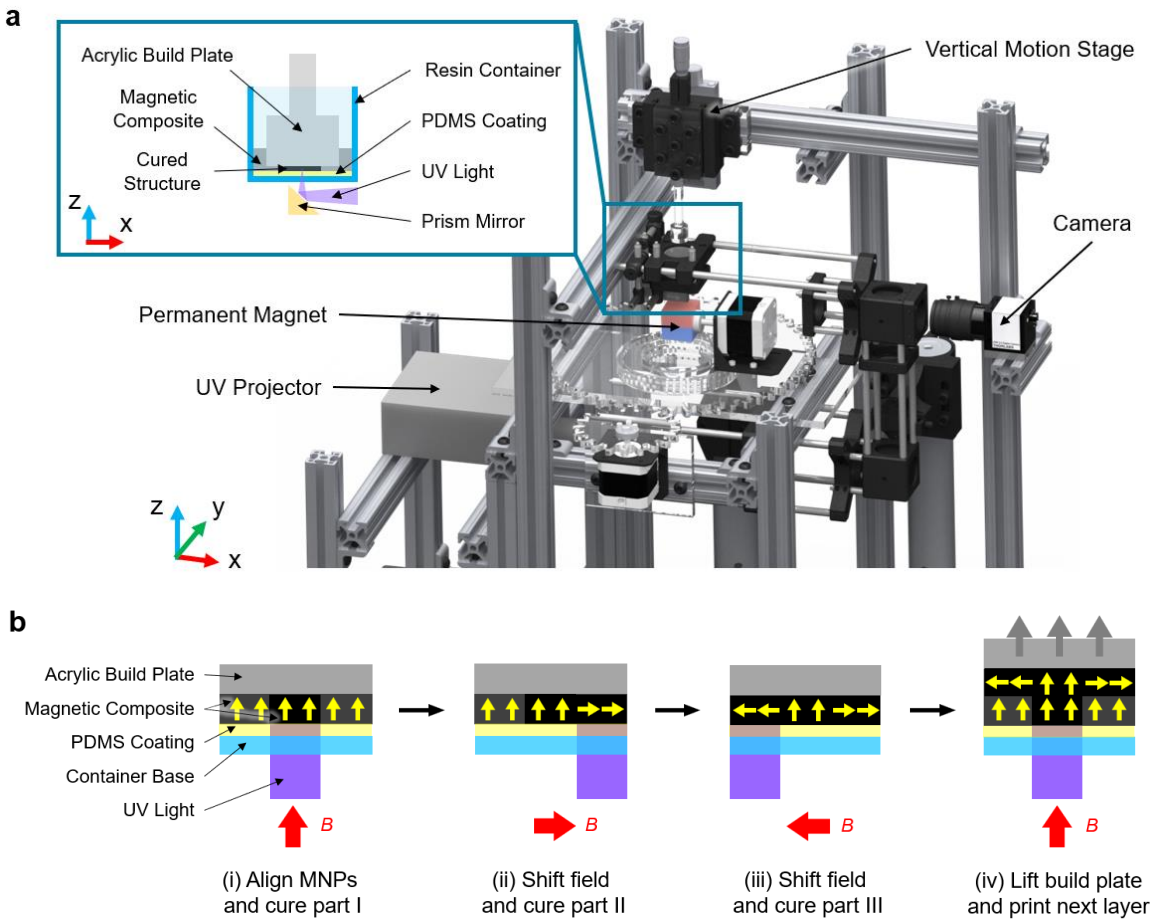

Figure 1. (a) Schematic representation of fabrication system. The inset shows the sectional view of build plate, resin container and prism mirror. The vertical motion stage can be adjusted to move along *z* axis to lift the build plate. The image of the real apparatus is shown in Figure S1. (b) Process of multi-layer printing. The yellow arrows within magnetic composite indicate the magnetization directions. The cured and uncured segments of magnetic composite are shown in black and gray, respectively. Red arrows represent the directions of alignment field *B*, and gray arrows in step (iv) represent the lifting direction of the build plate.

2. Results

2.1. Multi-layer Printing with Magnetization Encoding

Extended from the method of printing 2D folded magnetic shapes using DLP in our previous work,[27] multi-layer miniature soft robots were fabricated by vertically stacking layers of magnetic patterns in this paper. A bottom-up printing method was used, where the resin is cured through a window in the bottom of the resin vat by a light source from below. As is common in standard (non-magnetic) DLP-based 3D printers, the build platform within the vat is raised sequentially after each layer is completed, to enable multi-layer structure printing. The magnetization of individual regions within layers is encoded by orienting embedded MNPs during selective curing of discrete zones using projected UV light patterns.

2.1.1. Fabrication System

Figure 1(a) shows the physical system for printing 3D magnetic shapes with discrete magnetization profiles. The magnetic composite, comprised of NdFeB nanoparticles within a UV photopolymer, is filled into a small resin container. The resin container has a transparent base made of acrylic, which allows the light pattern projected from UV light source to be transmitted through. During printing, the light pattern travels through a series of lenses and mirrors and gets focused on the curing zone within the vat which is located directly above the base window.

To align the embedded MNPs within the resin to allow for patterned magnetization of a target region, a large magnetic field is induced at the build site by a permanent cubic magnet which is placed below the prism mirror. The advantage of placing this cubic magnet below the resin container (as opposed to other arrangements such as placing this magnet to the side which would allow for easier optical paths) is that this magnetic location keeps the MNPs from being pulled laterally during curing that would distort the MNPs' uniformity within the cured structures. Placing the permanent magnet directly below the resin container would block the optical path of UV light as the light is projected from below either. However, the permanent magnet needs to be placed in close proximity to the curing zone to ensure large alignment field, hence a small-sized prism mirror is inserted in between to bring the projected light pattern in from the side. The relation between this alignment field magnitude and separation distance as well as the relation between field angle and orientation of magnet is shown in Figure S2. To ensure a large alignment field as well as prevent collision between the permanent magnet and the prism mirror, the smallest separation distance that can be achieved from magnet's center of mass to the curing zone is set to 3.25 cm. With this separation distance, the projected alignment field measured at the curing zone ranges from 48 mT to 84 mT depending on the orientation of the magnet, which is shown as Figure S2(c).

To define a single layer thickness during the printing process, a small gap is formed between the base of the container and the build plate. The build plate is mounted on a linear motion stage and can be lifted by adjusting the vertical position. The cured structures need to be detached from the base when lifting the build plate for multi-layer stacking, thus, a PDMS film is coated on top of the base to reduce such adhesion.

Figure 1(b) shows the process of manufacturing multi-layer magnetic structures with magnetization encoding. The pre-magnetized embedded MNPs were first oriented by the alignment field, at which time the UV light was projected to mechanically fix the magnetization direction by polymerizing the selected regions and freezing nanoparticles' orientations. After the selected region was cured, the build plate was lifted for a small distance to create a new gap with the cured structure attached. The surrounding magnetic slurry flowed in and filled the gap due to its weight. Subsequent layers were printed by repeating the same procedure discussed above.

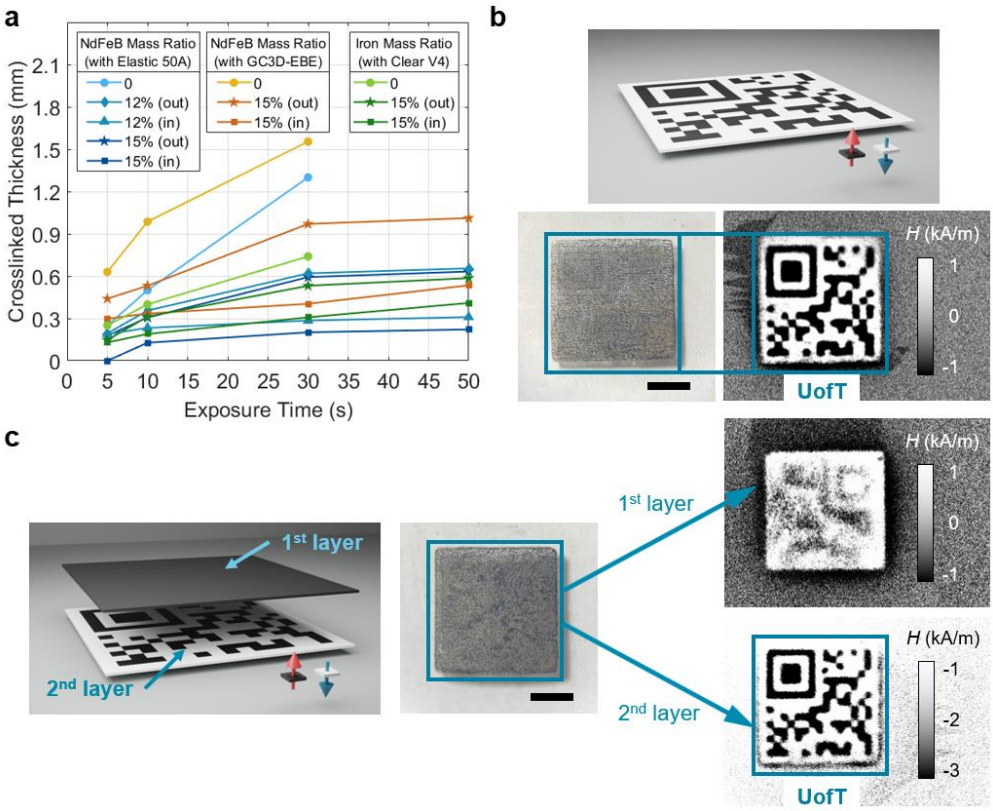

Figure 2. (a) Crosslinked thickness of magnetic composite. Three types of magnetic composites are studied here, of which the types of MNPs and polymer matrix are shown in the title box of each legend. The "in" and "out" represent "in-plane" and "out-of-plane" magnetization, respectively. Zero thickness implies the printed sample is not cured or fully cured. (b) Single-layer square structure with encoded magnetization of micro QR code. The black and white pixels represent the magnetization directions of 0° and 180°, as indicated by

the red and blue arrows. (c) Double-layer square structure with magnetization of 0° on the first layer and micro QR code on the second layer. The magnetization patterns of first and second layers are scanned using the MagView from top side and bottom side, respectively. Scale bar, 2 mm.

2.1.3. Crosslinked Thickness

Because the polymer matrix is only partially transparent (due to embedded MNPs), the UV light is attenuated as it travels through the slurry, leading to a crosslinked polymer thickness which is dependent on the powder loading ratio as well as the curing time. This crosslinked thickness is crucial to determining the layer-lifting distance in multi-layer fabrication. A lifting distance which is too large can cause fracture of printed structures, whereas a small lifting distance may result in programming interference between adjacent layers. Therefore, the lifting distance is set to 75~85% of the calibrated crosslinked thickness during layer stacking, which has been observed to maintain the bonding of adjacent layers while preventing programming interference between layers.

The magnetic material is composed of MNPs and UV photopolymer. NdFeB or iron particles were used as MNPs, which served as magnetically hard (permanent) or soft (non-permanent) particles, respectively. UV polymers with different flexural modulus including FormLabs Clear V4 (~6.91 GPa), FormLabs Elastic 50A (~0.30 GPa) and GC3D-EBE Flexible (~0.12 GPa)[44] were chosen to meet different structural requirements under various experimental scenarios. Three types of magnetic composites were studied here with different combinations of MNPs and photopolymer, which include two flexible hard magnetic composites (NdFeB nanoparticles mixed with FormLabs Elastic 50A or GC3D-EBE Flexible) and one rigid soft magnetic composite (iron particles mixed with FormLabs Clear V4).

The crosslinked thickness varies for different polymer matrices. Meanwhile, the transparency of the composite varies for different mass fractions of MNPs, which affects the crosslinked thickness of the structure layer when being exposed to UV light. Another factor that impacts the crosslinked thickness is the orientation of embedded nanoparticles, whether “in-plane” or “out-of-plane” with respect to the horizontal plane. Figure 2(a) shows the crosslinked thickness with varying mass fractions of MNPs under different exposure time. Here the crosslinked thickness was tested for plain UV polymer as well as magnetic composites with different mass ratios and orientations of embedded MNPs. Square samples with size of 4 mm by 4 mm were printed for the thickness measurement using a micrometer.

Based on the measured result, the crosslinked thickness increases as the exposure time increases. For the same type of composite, the thickness decreases as the mass ratio of

embedded MNPs increases. In addition, the “in-plane” orientation shows lower crosslinked thickness than the “out-of-plane” orientation under the same condition.

2.1.3. Evaluation of Magnetization Encoding

The magnetization of the robot segments is controlled by orienting embedded MNPs using the alignment field in sequence. However, features that were already printed can themselves locally generate a magnetic field, which in some cases affect subsequent MNPs’ reorientation processes in nearby features within the same layer and segments in subsequent layers. Such magnetic interaction can cause inaccuracy in magnetization encoding. To assess the degree of such influence, the encoding result of magnetization is evaluated by reading the magnetic polarity using magneto-optical sensor (MagView S, Matesy GmbH, Germany) for both single-layer and double-layer structures.

For a single-layer structure, we project a 6 mm by 6 mm square pattern of micro QR code to the magnetic composite and encode black and white phases by orienting embedded NdFeB particles in 0° and 180° “out-of-plane” magnetization directions, respectively. The projected pattern is shown in Figure 2(b), showing a magnetization resolution of 350 μm. By visualizing the magnetization pattern of fabricated square samples using the MagView, a clear pattern of micro-QR code is generated and the character string of “UofT” can be successfully scanned.

To test the ability to accurately program a two-layer structure, the first layer is given a uniform 0° “out-of-plane” magnetization across its entire surface, while the magnetization of the second layer is encoded with the same micro QR code as single-layer structure. By observing each side with the MagView, magnetization profiles for both layers of the double-layer structure can be displayed as Figure 2(c). In the visualization process of the second layer, the first layer also projects magnetic fields that can be captured by the MagView, thus generating a net magnetization direction towards 0° and shifting the displayed pattern towards darker spectrum. Figure S4 shows the magnetization profiles for both single-layer and double-layer structures under the same field range. It is observed that the QR code pattern of the double-layer structure is darker than the single-layer structure. Therefore, the field range of the QR code pattern is shifted by –2 kA/m in Figure 2(c), and the character string of “UofT” can still be successfully scanned after field shifting.

The high resolution of magnetization encoding for both single-layer and double-layer structures indicates that the external alignment field is dominant in orientating the embedded MNPs, and the magnetic effect of formerly printed features on subsequent features is

negligible. Therefore, the magnetic polarity across multiple layers can be created with high precision using such magnetization approach.

2.1.4. Integration of Multiple Materials

Multiple materials with different stiffness and magnetic properties were integrated to enhance the functionality and complexity of fabricated robots. The integration of multiple materials can be achieved by switching resin type during fabrication. Locking docks were added on the positioning stage to secure the build plate during the switching process, which ensures the consistency of build plate's position during material switching and the alignment of projected light patterns for different materials. The build plate was extracted out of the workspace and cleaned by flushing away uncured composites when changing materials. The build plate with cured structure was then placed back for the printing of next material.

Soft magnetic material (SMM) such as iron exhibits lower coercivity and higher permeability than hard magnetic material (HMM) such as NdFeB. While SMM cannot be programmed with a fixed magnetization direction, application of an alignment field during curing will align the particles of SMM in chains along the applied field axis. These chains induce an "easy" magnetization axis, which is a preferential magnetization axis.[16,45-47] This easy axis of magnetization can be switched forwards/backwards by applying the actuating field in an oscillating manner. Based on such easy-axis property, a segment made of SMM can be used as orientation-anchoring mechanism to fix the heading angle of the robot while the segment made of HMM can be used to exhibit reciprocal motions under oscillatory field signals.

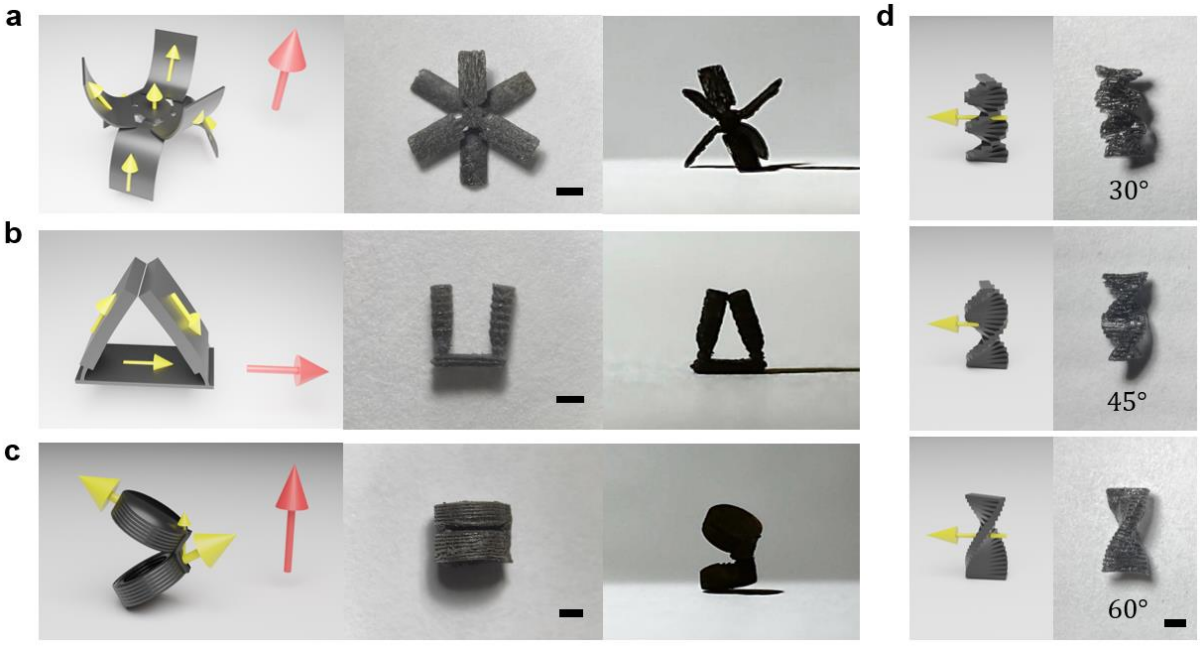

Figure 3. 3D-printed robots with encoded magnetization profiles and shape transformation under magnetic actuation. Yellow arrow represents the magnetization direction at each

segment and red arrow represents the direction of actuation field. The magnitude of actuation field is 30 mT. (a) Stool-shaped robot. (b) Gripper-shaped robot. (c) Capsule-like robot. (d) Helical robots with helix angles of 30°, 45° and 60°. Scale bar, 1 mm.

2.2. 3D-printed Multi-layer Structures

Compared with 2D folded shapes, 3D structures have better performance in terms of robustness and kinematic flexibility. For example, capillary force plays an essential role in the actuation of 2D folded soft robots, which may cause the robot to adhere to the inner surface of the workspace. However, the actuating part of 3D structures can assume a larger volume and more complex geometry, thus having greater force and smaller contact area to overcome the capillary effect.

Figure 3 shows printed 3D structures including stool-shaped, gripper-shaped, capsule-like and helical robots which use the magnetic composite made of NdFeB nanoparticles and Elastic 50A photopolymer. The stool-shaped robot consists of 3 layers, where the top and bottom layers are encoded with anisotropic magnetization and the middle layer is used for conjunction. The structure gets deformed into a stool shape when actuated by the external magnetic field, which is shown as Figure 3(a).

The gripping arms of gripper-shaped robot are printed by stacking layers of rectangle patterns with the smallest width of 200 μm, which demonstrates the capability of aligning and stacking small features along vertical direction using such fabrication method. Meanwhile, the dimension of the feature can be precisely controlled during stacking. As Figure 3(b) shows, the arm is thinner at the joint part for higher flexibility and wider at the link part to get a greater actuating torque.

2.2.1. Capsule-like Robot

Capsule-like robots are promising robotic tools in untethered drug delivery or biological sampling.[48] We print a capsule-like robot by stacking ring shapes along the height of the cylinder with two solid circles at both ends. Small rectangular patterns are stacked vertically to form the backbone. The volume of the backbone needs to be small to ensure the bending flexibility when opening and closing the caps. One layer of ring is skipped in the middle to create the gap between two caps. A small supporting beam is added in between to prevent the structural delamination during build plate lifting.

Figure 3(c) shows the magnetization profile of the robot. The net magnetic moment is pointing along the height of the cylinder. In the idle state, two caps attract each other due to magnetic interaction, which forms its “closed” state. When deployed into actuation field, the caps align themselves with the external field due to magnetic torque and shift into “open”

state. The relation between the opening angle and the applied field is shown as Figure 4(a). It is observed that the opening angle of the capsule is zero when the external field is lower than 3 mT. Therefore, a small field can be applied to steer the robot without opening the caps. The opening angle increases as the applied magnetic field increases and becomes stable when the field strength is greater than 35 mT.

Figure 4(b) shows the actuation of the capsule-like robot in a maze map. The robot can achieve the procedure of cargo gripping, transporting, and releasing. During the process of gripping and releasing, a uniform magnetic field of 25 mT within horizontal plane was applied to open the caps of the robot. A small field along the vertical axis was superimposed to generate tumbling motion for the capsule to approach the cargo. The robot got into "closed" state with two caps attracting each other when the external field was removed, thus gripping the cargo tightly. Then a rotating magnetic field of 2 mT was applied to rotate the capsule and transport the cargo to the other end of the maze map. The uniform field of 25 mT was applied again to open the caps of the robot for cargo releasing. Such procedure can also be used to sample and transport swarm of small particles.

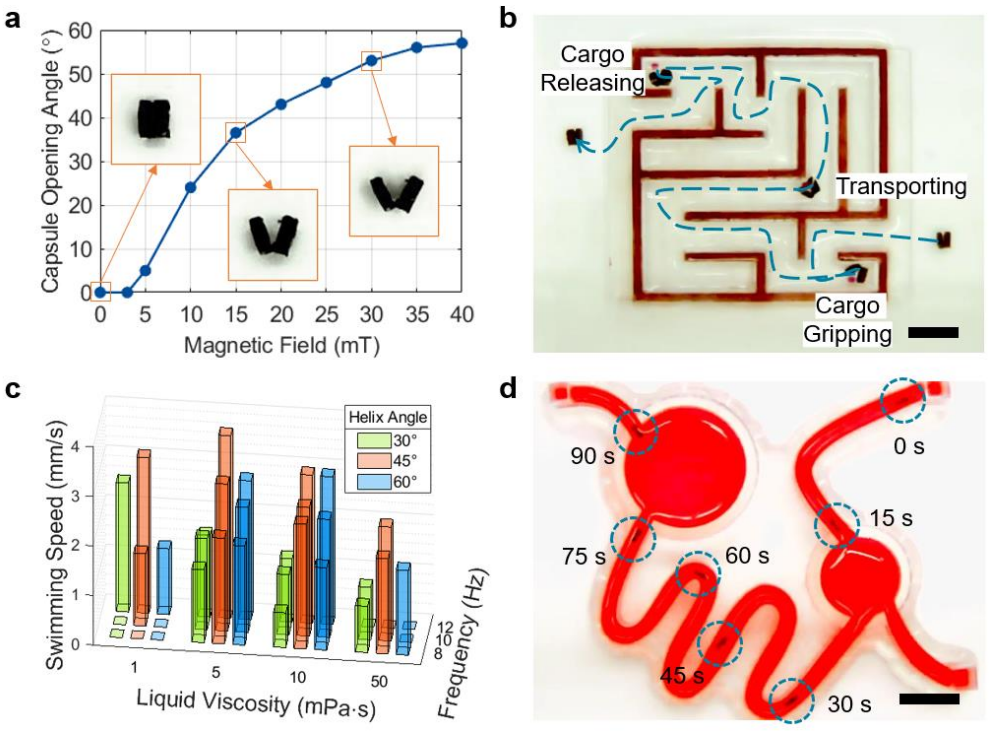

Figure 4. (a) Opening angle of capsule-like robot under applied magnetic field. The insets illustrate the patterns of capsule opening under magnetic fields of 0, 15 mT and 30 mT. (b) Navigation of capsule-like robot in a maze map for cargo manipulation including gripping, transporting, and releasing. (c) Swimming speed of helical robots with different helix angles. The robots are deployed into fluids with different viscosities and get actuated under different rotational frequencies. Occurrence of tumbling motion results in zero swimming speeds at

viscosity of 1 mPa·s, and the "step-out" phenomenon causes zero speeds at viscosity of 5 mPa·s. (d) Navigation of helical robot in a vascular model. Scale bar, 2mm.

2.2.2. Helical Robot

Previous studies have investigated magnetic microswimmers with helical or twist-type geometries that can be actuated under rotating magnetic field to swim in liquid environments.[2-4,7-9,14] In this work, helical robot with height of 4 mm and diameter of 2 mm was fabricated by stacking 20 layers of rectangles along its height. The thickness of each layer is 0.2 mm. The helix angle is controlled by the twisting angle between adjacent layers. Figure 3(d) shows the fabricated helical robots with helix angles of 30, 45 and 60 degrees, respectively. All layers have "in-plane" magnetization with the same direction; thus, the magnetic moment of the helical robot is along its geometric short axis. By applying a rotating field with high frequency, the helical robot can rotate along its long axis and generate propulsive force in liquid environment.

We measured the swimming speed of helical robots by navigating the helical robots in a 3D printed channel. The helical robots were deployed into the electromagnetic coil system and actuated by a rotating magnetic field with the amplitude of 16 mT. Figure 4(c) shows the measured swimming speeds of helical robots under rotational frequencies of 8 Hz, 10 Hz and 12 Hz in liquids with different viscosities. The helical robot exhibits tumbling motion under low rotational frequency and liquid viscosity, which prevents it from propulsion. When the liquid viscosity or the rotational frequency increases, with a tumbling motion, the fluidic drag on the robot becomes larger, thus transforming its rotation along the geometric short axis to the long axis. In this way, the propulsive force is generated to propel the robot for swimming. The "step-out" occurs when the rotational frequency and liquid viscosity become high, thus impeding propulsion.

Figure S5 shows the swimming patterns of helical robots in the liquid with viscosity of 5 mPa·s. The robots with different helix angles were actuated under three rotational frequencies. The swimming speed increases as the rotational frequency increases. It is observed that the helical robot with helix angle of 45° has higher swimming speeds than the other two angles. Therefore, we deployed such robot into a vascular model and successfully navigated it from one end to the other using rotating field with rotational frequency of 12 Hz, which is shown as Figure 4(d). The direction of robot's propulsion is controlled by steering the plane where the rotating field lies.

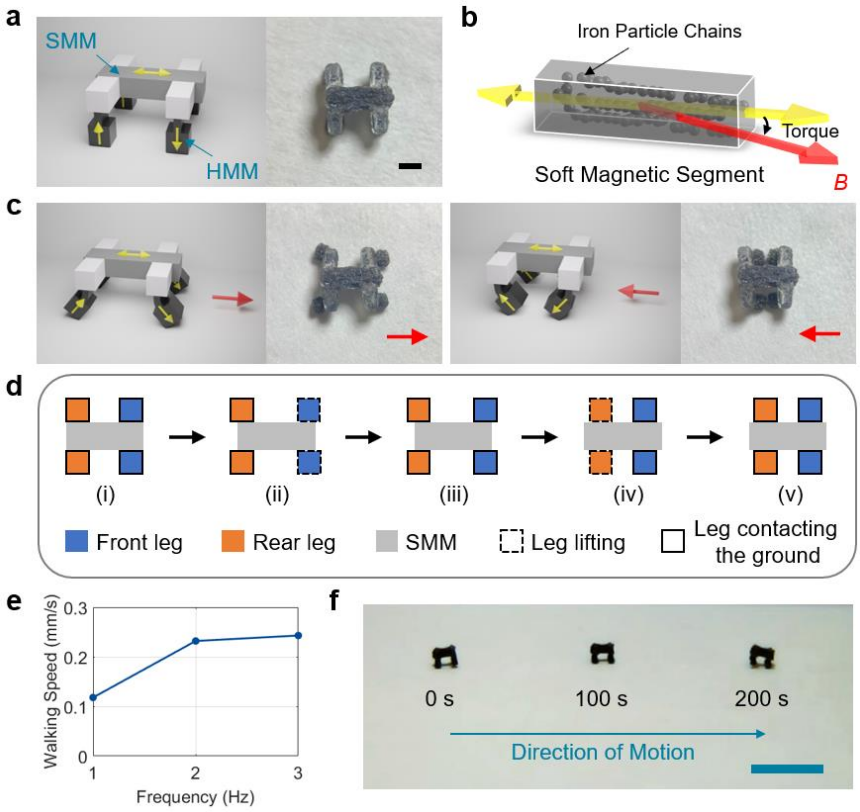

Figure 5. Walking robot made of SMM and HMM. (a) Schematic representation of walking robot in the idle state. Segments made of SMM and HMM are in gray and black, respectively. The white segment represents the non-magnetic part made of plain UV photopolymer. Yellow arrow represents the magnetization direction at each segment. Scale bar, 1 mm. (b) Illustration of soft magnetic segment with embedded iron particle chains aligned along the geometric long axis. The bidirectional yellow arrow indicates the alignment direction of iron particle chains. Cooperative torque is generated when the external field *B* is applied. (Note: Iron particles in the figure are only for the illustration purpose of particle chain and are not drawn here to scale.) (c) Deformation of robot's legs under magnetic field. The forelegs and rear legs bend towards and away from each other while the orientation of the robot keeps constant as the field direction switches by 180°. Red arrow represents the direction of applied magnetic field. The magnitude of applied field is 50 mT. (d) Demonstration of walking gait in a gait cycle from top view. Step (i) shows the gait in the idle state, and the robot moves towards right by circulating step (ii) to step (v). (e) Walking speed of the robot in oscillating magnetic field with different frequencies. (f) Motion of the robot under actuation field with oscillatory frequency of 2 Hz. Scale bar, 10 mm.

2.2.3. Walking Robot

A walking robot with four legs was fabricated by integrating SMM and HMM, as well as rigid and flexible polymer matrices. As discussed previously, SMM has low coercivity and can

induce a large magnetic moment in an applied field, which makes it a great candidate as orientation-anchoring mechanism under oscillating field signals. As Figure 5(a) shows, the main body of the walking robot is made of rigid SMM while the legs are made of flexible HMM. For each leg, the width of the link is greater than the joint for a larger deformation. Meanwhile, the volume of the soft magnetic segment needs to be large to ensure the induced magnetic moment of soft magnetic segment is greater than that of deformed hard magnetic segments, thus making the net magnetic moment align with the external field and exhibit the anchoring characteristic. The induced magnetic moment points along the alignment direction of particle chains, so the embedded iron particles are reoriented to align along the geometric long axis of the soft magnetic segment, which is shown as Figure 5(b). Cooperative torque can be generated on the soft magnetic segment to correct the heading angle if it deviates from the direction of applied field. The shoulder parts are made of plain UV photopolymer GC3D-EBE Flexible for better deformation performance due to its low flexural modulus.

The oscillating magnetic field to actuate the walking robot is applied within the horizontal plane and has the pattern of sinusoidal wave with the amplitude of 40 mT. Fields with magnitude lower than 10 mT are filtered because small fields cannot induce large magnetic moment on soft magnetic segment but generate magnetic torques on deformed hard magnetic segments, which may cause the reversal of robot's orientation.

By applying such oscillating field along the geometric long axis of soft magnetic segment, the forelegs and rear legs made of HMM swing towards and away from each other while the heading angle remains consistent. To make the robot walk, small field components along the vertical axis are superimposed to tilt the body of the robot periodically. A walking gait is formed as Figure 5(d) shows, which induces the robot to walk towards the right. The heading angle of the robot can be steered by rotating the plane where the oscillating field lies. Figure 5(e) measures the walking speed of the robot under different oscillatory frequencies. The "step-out" occurs when the frequency is higher than 3 Hz.

3. Discussion

In this paper, we developed a fabrication approach to 3D print millimeter-scale magnetic structures with encoded magnetization profiles. Structures with complex shapes can be produced within minutes using stereolithography. The digital process also enables the manufacturing of 3D miniature robots with high degree of automation and reproducibility. Table S1 summarizes the features of fabricated robots discussed in this work.

Compared with single-layer structures, multi-layer printing explores a wider spectrum for robot designs and greatly enhances the structural complexity. Meanwhile, large magnetic

torques can be generated by stacking thick features or multiple layers for deforming parts, which is not achievable in single-layer fabrication, thus contributing to a higher strength for actuation. Moreover, integration of multiple materials with different stiffness and magnetic properties enhances the functionality and maneuverability of printed structures.

However, the presented fabrication approach has limitations in terms of the intensity and continuity of magnetization. The magnetization is formed by orienting pre-magnetized NdFeB nanoparticles using alignment field with moderate strength (48~84 mT). Thus, the intensity of magnetization is lower compared with the one-time magnetization using saturated field (2~3 T). Consequently, the magnitude of structural deformation for printed shapes under actuation is limited. Moreover, compared with one-time magnetization to form continuous magnetization on pre-deformed shapes, the presented method requires a longer time to form a smooth and continuous magnetization profile as the magnetization is discretely patterned for each individual segment.

Future work will explore the incorporation of multiple materials with different stimuli. Meanwhile, biocompatibility of the material will be studied combined with in-vitro or ex-vivo tests using printed robots, such as transporting drug particles to the wound of biological tissues using capsule-like robot or navigating helical robots coated with thrombolytic drugs to dissolve blood clots at target locations.

4. Experimental Section/Methods

Materials: Various types of magnetic materials were prepared by mixing NdFeB or iron particles with different polymer matrices. For flexible hard magnetic material (HMM), the permanent magnetic particles (D50 = 5 microns, MQFP-15-7, NdPrFeB, Magnequench (Tianjin) Co. Ltd., Tianjin, China) were first magnetized in a strong uniform magnetic field (2.4 T) generated by an impulse magnetizer (9 Tesla Pulse Magnetiser, Magnetic Measurements Ltd., Lancashire, UK) to get the saturation remanence. They were then mixed with flexible UV resin (Elastic 50A, Formlabs Inc., MA, USA or GC3D-EBE Flexible Beige, Smart Your Life, Taiwan). For rigid soft magnetic material (SMM), the iron particles (Iron Metallic Powder -325Mesh, Sculpture Supply Canada, Canada) were mixed with rigid UV resin (Clear V4, Formlabs Inc., MA, USA). 1% w/w fumed silica (S5130-100G, Sigma-Aldrich Canada Co., Canada) was added to the magnetic composite to homogenize the distribution of embedded MNPs and prevent particle aggregation during printing. The mixed composite was then stirred by a glass rod for 5 minutes to form a homogeneous magnetic slurry. After removing bubbles in a vacuum degassing chamber for 1 minute, the magnetic slurry was transferred into a cylindrical resin container. The container is composed of 3D

printed walls and a base made of clear acrylic plastic (Clear Scratch- and UV-Resistant Cast Acrylic Sheet, McMaster Carr, OH, USA). A polydimethylsiloxane (PDMS) (SYLGARD 184, The Dow Chemical Company, USA) film with thickness of ~1 mm was coated on top of the container base to reduce the adhesion between cured parts and the base when detaching layer during lifting. The polymeric base and curing agent of PDMS were thoroughly mixed with the mass ratio of 10:1. The mixture was then poured into the container and took 24 hours to get cured and form the coating.

Magnetic composite made of NdFeB nanoparticles and FormLabs Elastic 50A was used for the fabrication of stool-shaped, gripper-shaped, capsule-like and helical robots. For the walking robot, the rectangular body was first printed using SMM made of iron particles and FormLabs Clear V4 and followed by printing the shoulder parts using plain photopolymer GC3D-EBE Flexible. Then the legs were printed using flexible HMM made of NdFeB nanoparticles and GC3D-EBE Flexible.

Fabrication: The resin container filled with magnetic composite was placed above the prism mirror in the fabrication system. The UV light pattern was generated from a DLP projector (DLP LightCrafter 4500, modified with a 405-nm light engine, Texas Instruments Inc., TX, USA). The light beam was transmitted through a series of convex lenses (LA1608-A/ LA1509/LA1986, Thorlabs Inc., NJ, USA) and focused on the curing zone. The embedded MNPs were oriented by the alignment field generated by a cubic permanent magnet below the prism mirror. After that, the region of interest was exposed to the blue light (405 nm, 80 lx) to fix the magnetization direction. The duration of exposure time depends on the desired crosslinked thickness. The reorienting and curing steps were alternated for more cycles to create the customized magnetization profile. The build plate was extracted out of the vat after all curing steps and then washed by IPA (Isopropyl Alcohol 99.5%+, Caledon Laboratories Ltd., ON, Canada) to remove uncured materials. For multi-material printing, the material in resin container was first changed, and then the build plate was mounted back on the vertical motion stage for the printing of next material. Finally, the build plate with the finished structure was immersed in IPA for 2 minutes and the cured structure was then detached from the build plate by needles.

Actuation: Electromagnetic coil system with 8 degrees of freedom (DOF) was used for the robot actuation, which is shown as Figure S6. The printed robots were actuated in the plane 10 cm above the tabletop. The magnetic field was modulated by a joystick. The videos and images were captured by two CMOS cameras mounted on top and to the side.

Supporting Information

Supporting Information is available from the Wiley Online Library or from the author.

Acknowledgements

The authors gratefully acknowledge the financial support provided by the Natural Sciences and Engineering Research Council of Canada (NSERC). The authors also thank Adam Schonewille for building the 8-DOF electromagnetic coil system used in this work.

Received: ((will be filled in by the editorial staff))

Revised: ((will be filled in by the editorial staff))

Published online: ((will be filled in by the editorial staff))

References

[1] N. Xia, D. Jin, V. Iacovacci, L. Zhang, *Multifunctional Materials* **2022**, *5*, 012001.

[2] U. Bozuyuk, O. Yasa, I. C. Yasa, H. Ceylan, S. Kizilel, M. Sitti, *ACS Nano* **2018**, *12*, 9617.

[3] Y. Liu, Y. Yang, X. Yang, L. Yang, Y. Shen, W. Shang, *Journal of Materials Chemistry B* **2021**, *9*, 1441.

[4] J. Nam, W. Lee, J. Kim, G. Jang, *IEEE/ASME Transactions on Mechatronics* **2017**, *22*, 2461.

[5] J. Zhang, Z. Ren, W. Hu, R. H. Soon, I. C. Yasa, Z. Liu, M. Sitti, *Science Robotics* **2021**, *6*.

[6] S. Kim, F. Qiu, S. Kim, A. Ghanbari, C. Moon, L. Zhang, B. J. Nelson, H. Choi, *Advanced Materials* **2013**, *25*, 5829.

[7] G. Hwang, A. J. Paula, E. E. Hunter, Y. Liu, A. Babeer, B. Karabucak, K. Stebe, V. Kumar, E. Steager, H. Koo, *Science Robotics* **2019**, *4*.

[8] I. S. Khalil, D. Mahdy, A. E. Sharkawy, R. R. Moustafa, A. F. Tabak, M. E. Mitwally, S. Hesham, N. Hamdi, A. Klingner, A. Mohamed, M. Sitti, *IEEE Robotics and Automation Letters* **2018**, *3*, 1112.

[9] X. Yan, Q. Zhou, M. Vincent, Y. Deng, J. Yu, J. Xu, T. Xu, T. Tang, L. Bian, Y.-X. J. Wang, K. Kostarelos, L. Zhang, *Science Robotics* **2017**, *2*.

[10] R. H. Soon, Z. Ren, W. Hu, U. Bozuyuk, E. Yildiz, M. Li, M. Sitti, *Proceedings of the National Academy of Sciences* **2022**, *119*.

[11] C. Hong, Z. Ren, C. Wang, M. Li, Y. Wu, D. Tang, W. Hu, M. Sitti, *Science Robotics* **2022**, *7*.

[12] Z. Liu, M. Li, X. Dong, Z. Ren, W. Hu, M. Sitti, *Nature Communications* **2022**, *13*.

[13] S. Kim, S. Lee, J. Lee, B. J. Nelson, L. Zhang, H. Choi, *Scientific Reports* **2016**, *6*.

[14] X. Wang, X.-H. Qin, C. Hu, A. Terzopoulou, X.-Z. Chen, T.-Y. Huang, K. Maniura-Weber, S. Pané, B. J. Nelson, *Advanced Functional Materials* **2018**, *28*, 1804107.

[15] M. Soreni-Harari, R. St. Pierre, C. McCue, K. Moreno, S. Bergbreiter, *Soft Robotics* **2020**, *7*, 59.

[16] C. Peters, O. Ergeneman, P. D. García, M. Müller, S. Pané, B. J. Nelson, C. Hierold, *Advanced Functional Materials* **2014**, *24*, 5269.

[17] Y. Kim, H. Yuk, R. Zhao, S.A. Chester, X. Zhao, *Nature* **2018,** *558*, 7709.

[18] C. Ma, S. Wu, Q. Ze, X. Kuang, R. Zhang, H. J. Qi, R. Zhao, *ACS Applied Materials & Interfaces* **2020**, *13*, 12639.

[19] S. Wu, C. M. Hamel, Q. Ze, F. Yang, H. J. Qi, R. Zhao, *Advanced Intelligent Systems* **2020**, *2*, 2000060.

[20] S. Sundaram, M. Skouras, D. S. Kim, L. van den Heuvel, W. Matusik, *Science Advances* **2019**, *5*.

[21] P. Lloyd, A. K. Hoshiar, T. da Veiga, A. Attanasio, N. Marahrens, J. H. Chandler, P. Valdastri, *IEEE Robotics and Automation Letters* **2020**, *5*, 3937.

[22] J. Zhang, E. Diller, *Soft Robotics* **2018**, *5*, 761.

[23] H. Gu, Q. Boehler, H. Cui, E. Secchi, G. Savorana, C. De Marco, S. Gervasoni, Q. Peyron, T.-Y. Huang, S. Pane, A. M. Hirt, D. Ahmed, B. J. Nelson, *Nature Communications* **2020**, *11*.

[24] G. Shao, H. O. Ware, J. Huang, R. Hai, L. Li, C. Sun, *Additive Manufacturing* **2021**, *38*, 101834.

[25] G. Shao, H. O. Ware, L. Li, C. Sun, *Advanced Engineering Materials* **2020**, *22*, 2070009.

[26] X. Cao, S. Xuan, S. Sun, Z. Xu, J. Li, X. Gong, *ACS Applied Materials & Interfaces* **2021**, *13*, 30127.

[27] T. Xu, J. Zhang, M. Salehizadeh, O. Onaizah, E. Diller, *Science Robotics* **2019**, *4*.

[28] Z. Ji, C. Yan, B. Yu, X. Wang, F. Zhou, *Advanced Materials Interfaces* **2017**, *4*, 1700629.

[29] E. B. Joyee, Y. Pan, *Journal of Manufacturing Processes* **2020**, *56*, 1178.

[30] H. Shinoda, S. Azukizawa, K. Maeda, F. Tsumori, *Journal of The Electrochemical Society* **2019**, *166*.

[31] S. Lantean, G. Barrera, C. F. Pirri, P. Tiberto, M. Sangermano, I. Roppolo, G. Rizza, *Advanced Materials Technologies* **2019**, *4*, 1900505.

[32] Y. Alapan, A. C. Karacakol, S. N. Guzelhan, I. Isik, M. Sitti, *Science Advances* **2020**, *6*.

[33] L. Li, C. Xin, Y. Hu, R. Li, C. Li, Y. Zhang, N. Dai, L. Xu, L. Zhang, D. Wang, D. Wu, C. Liao, Y. Wang, *ACS Applied Materials & Interfaces* **2022**, *14*, 52370.

[34] X. Ke, S. Zhang, Z. Chai, J. Jiang, Y. Xu, B. Tao, H. Ding, Z. Wu, *Materials Today Physics* **2021**, *17*, 100313.

[35] Y. Dong, L. Wang, N. Xia, Z. Yang, C. Zhang, C. Pan, D. Jin, J. Zhang, C. Majidi, L. Zhang, *Science Advances* **2022**, *8*.

[36] J. Cui, T.-Y. Huang, Z. Luo, P. Testa, H. Gu, X.-Z. Chen, B. J. Nelson, L. J. Heyderman, *Nature* **2019**, *575*, 164.

[37] E. B. Joyee, Y. Pan, *Soft Robotics* **2019**, *6*, 333.

[38] Z. Ren, W. Hu, X. Dong, M. Sitti, *Nature Communications* **2019**, *10*.

[39] X. Dong, G. Z. Lum, W. Hu, R. Zhang, Z. Ren, P. R. Onck, M. Sitti, *Science Advances* **2020**, *6*.

[40] W. Hu, G. Z. Lum, M. Mastrangeli, M. Sitti, *Nature* **2018**, *554*, 81.

[41] C. Li, G. C. Lau, H. Yuan, A. Aggarwal, V. L. Dominguez, S. Liu, H. Sai, L. C. Palmer, N. A. Sather, T. J. Pearson, D. E. Freedman, P. K. Amiri, M. O. de la Cruz, S. I. Stupp, *Science Robotics* **2020**, *5*.

[42] J. C. Breger, C. K. Yoon, R. Xiao, H. R. Kwag, M. O. Wang, J. P. Fisher, T. D. Nguyen, D. H. Gracias, *ACS Applied Materials & Interfaces* **2015**, *7*, 3398.

[43] Q. Ze, X. Kuang, S. Wu, J. Wong, S. M. Montgomery, R. Zhang, J. M. Kovitz, F. Yang, H. J. Qi, R. Zhao, *Advanced Materials* **2020**, *32*, 2070025.

[44] Z. Li, E. Diller, *2022 International Conference on Manipulation, Automation and Robotics at Small Scales (MARSS)* **2022**.

[45] C. Peters, O. Ergeneman, B. J. Nelson, C. Hierold, *2013 IEEE 26th International Conference on Micro Electro Mechanical Systems (MEMS)* **2013**.

[46] J. Kim, S. E. Chung, S.-E. Choi, H. Lee, J. Kim, S. Kwon, *Nature Materials* **2011**, *10*, 747.

[47] H.-W. Huang, M. S. Sakar, A. J. Petruska, S. Pané, B. J. Nelson, *Nature Communications* **2016**, *7*.

[48] P. Shokrollahi, Y.P. Lai, S. Rash-Ahmadi, V. Stewart, M. Mohammadigheisar, L. Hubert, N. Matsuura, A.E.H. Zavodni, J. Parkinson and E. Diller, *IEEE/ASME Transactions on Mechatronics* **2021,** *26*, 2616.

Table of contents entry:

3D production of miniature soft robots that exhibit programmed shape transformation and controlled locomotion under magnetic actuation promotes application development in targeted or minimally invasive treatments. Multi-layer printing via digital light processing (DLP) provides a fast and precise way to produce sophisticated magnetic shapes. Discrete magnetization profiles are simultaneously formed by magnetization encoding.

Z. Li*, Y.P. Lai and E. Diller

3D Printing of Multi-layer Magnetic Miniature Soft Robots with Programmable Magnetization

ToC figure:

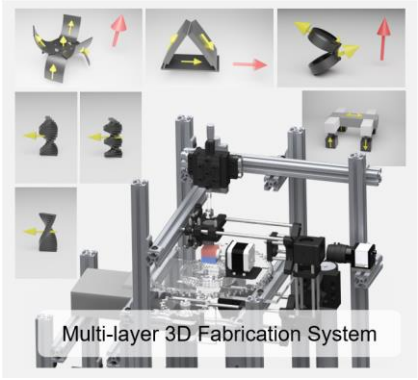

Supporting Information

3D Printing of Multi-layer Magnetic Miniature Soft Robots with Programmable Magnetization

Zhaoxin Li, Yung Priscilla Lai and Eric Diller*

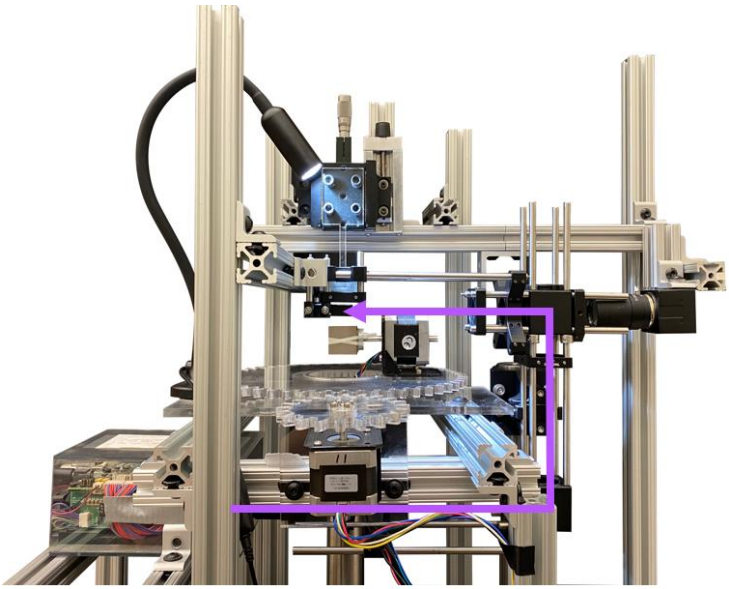

Figure S1. Physical apparatus of the fabrication system. Purple arrow represents the path of projected UV light beam.

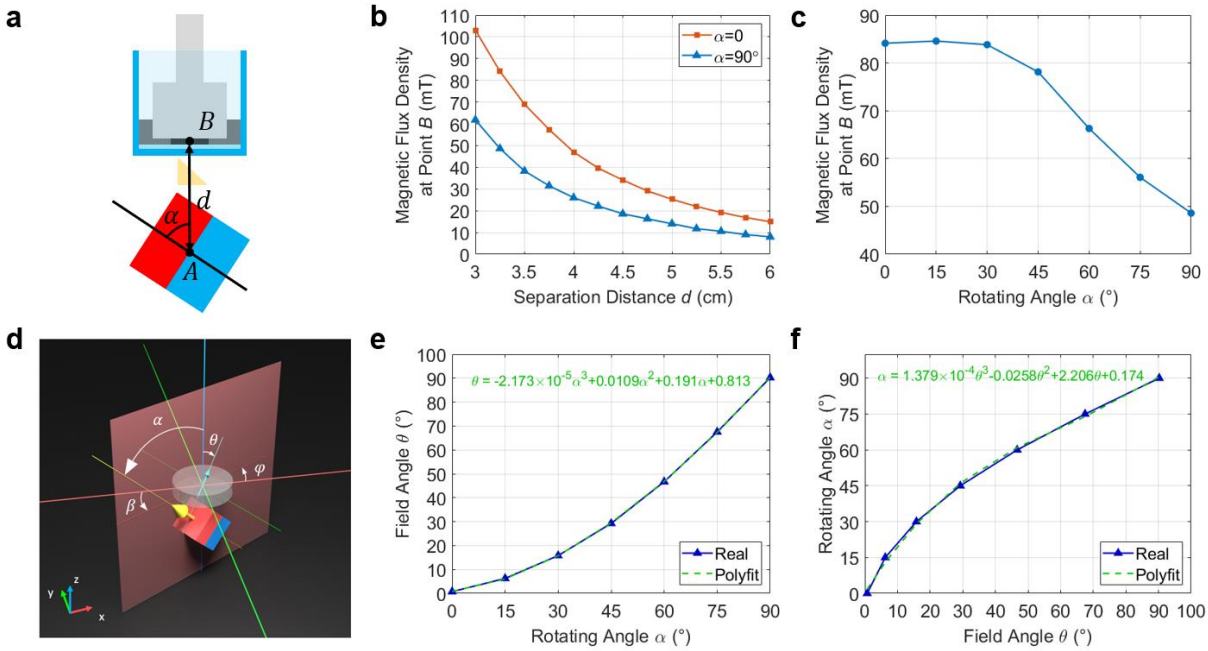

Figure S2. (a) Illustration of the rotating angle α of the permanent magnet and the separation distance d from magnet's center of mass to the curing zone. (b) Relation between the magnetic flux density at the curing zone and the separation distance d. (c) Relation between the magnetic flux density at the curing zone and the rotating angle α with the separation distance of 3.25 cm. (d) Illustration of azimuthal and polar angles of the magnetic field at the curing zone and the cubic magnet. (e) Relation between the field polar angle θ and the magnet polar angle α. Green curve represents the polynomial fitting curve. (f) Relation between the magnet polar angle α and the field polar angle θ. Green curve represents the polynomial fitting curve that is used to determine the rotating angle of the magnet based on the desired polar angle of the field.

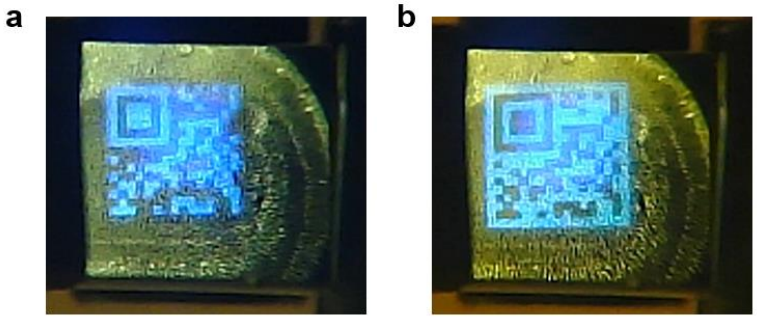

Figure S3. Projected UV pattern of micro QR code on curing zone. (a) Projected pattern with particles' orientation towards 0°. (b) Projected pattern with particles' orientation towards 180°.

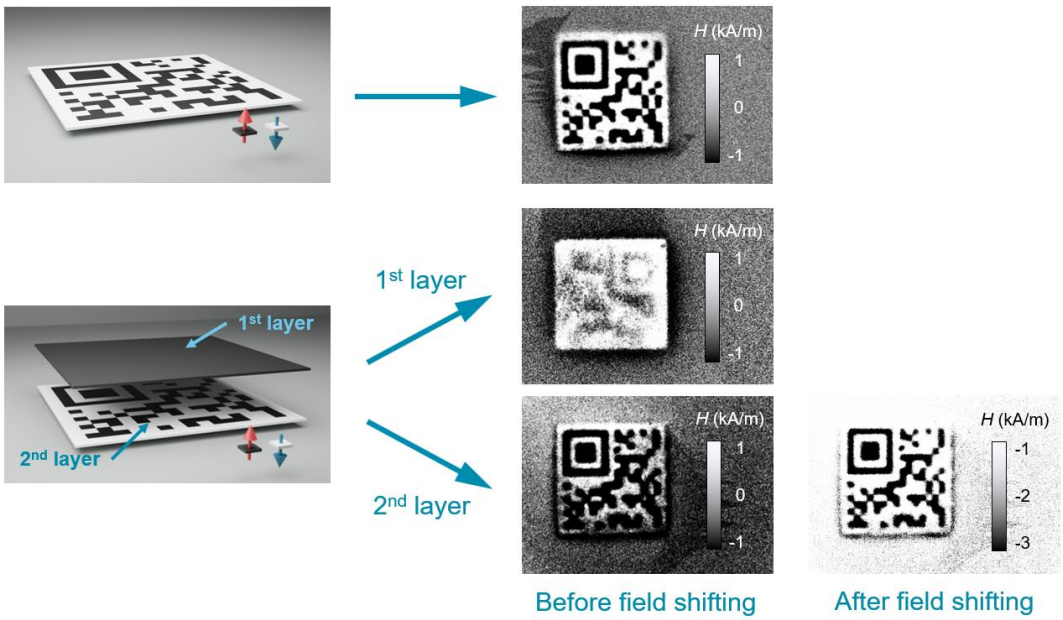

Figure S4. Magnetization profiles for single-layer and double-layer structures under the same field range as well as the magnetization profile of the second layer of double-layer structure after field shifting.

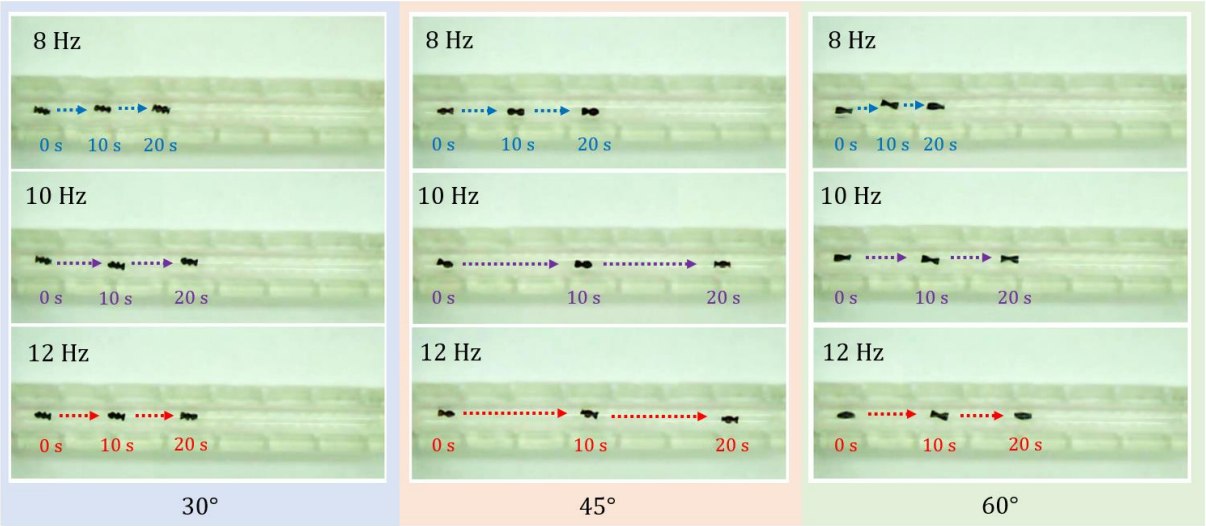

Figure S5. Motion of helical robots with different helix angles under different rotational frequencies in fluid with viscosity of 5 mPa·s. The video is shown in supplementary Movie S2.

Figure S6. 8-DOF electromagnetic coil system.

Table S1. Summary of fabricated robots discussed in this work.

Robot	Material Used	Number of Layers	Fabrication Time (min)[a)]	Functionality
Stool-shaped robot	NdFeB with Elastic 50A	3	3.5	Standing
Gripper-shaped robot	NdFeB with Elastic 50A	12	11	Gripping, tumbling, and releasing
Capsule-like robot	NdFeB with Elastic 50A	14	15.5	Gripping, rolling, and releasing
Helical robot	NdFeB with Elastic 50A	20	13.3	Swimming
Walking robot	NdFeB with GC3D-EBE Flexible, plain GC3D-EBE Flexible and iron with Clear V4	10	30	Walking

[a)]The fabrication time includes the time for MNPs' reorientation, material curing, build plate lifting, as well as the time of material switching for multi-material integration.